



Complementary conjugated piezo-phototronic polarized blue TiO₂ - KNN for piezophotocatalytic degradation of tetracycline enhanced under gentle oscillatory hydrodynamic disturbances

Yong Jieh Lee^a, Wei-Kean Chong^a, Lutfi Kurnianditia Putri^a, Boon-Junn Ng^a, Lling-Lling Tan^a, Ta Yeong Wu^a, Siang-Piao Chai^{a,*}

^a Multidisciplinary Platform of Advanced Engineering, Department of Chemical Engineering, School of Engineering, Monash University Malaysia, Jalan Lagoon Selatan, 47500 Bandar Sunway, Selangor, Malaysia

ARTICLE INFO

Keywords:

Piezophotocatalysis
Titanium dioxide
Potassium sodium niobate
Tetracycline

ABSTRACT

Recently, tetracycline (TC) is classified as an emerging contaminant due to its rapid discharge into the environment from anthropogenic sources. Piezophotocatalysis offers a unique solution to degrade TCs by collaboratively harnessing both solar and hydro energy. However, practical applications have been hampered by the necessitation of high energy requirement ultrasonic baths. In this work, BT-KNN conjugates were investigated for piezophotocatalytic TC degradation. Under agitation conditions, characterization studies demonstrated an amplified photocurrent, diminished charge transfer resistance and reduced radiative recombination. Concomitantly, BT-KNN composites exhibit enhanced TC degradation and apparent rate constant with increased fluid disturbance frequencies, illustrating 91.3% degradation in 3 h under gentle 4 Hz oscillations. These hydrodynamic disturbances engender a propitious piezopolarization which modulated the junction band bending and ameliorated the interfacial charge transfer, intensifying its performance. Optimization studies further illustrates the tradeoff dynamics between high photoactivity of BT and high piezo-enhancement of KNN.

1. Introduction

With the expeditious urbanization and industrialization, pollutants that were hitherto unheard of have become a commonplace occurrence. In particular, the reckless abuse of pharmaceutical bactericidal agents have led to the classification of antibiotic substances as an emerging pollutant. Tetracycline (TC), a broad spectrum prescribed antibiotic, has garnered significant attention due to its widespread applications in human medicine, livestock husbandry, veterinary, agriculture and aquaculture industry. Statistically speaking, tetracycline production amounts to 210,000 tons in China alone [1], with its regional usage accounting for approximately half the world's consumption [2]. Regrettably, tetracycline encounters an incomplete absorption and poor metabolic transformation within the body due to its hydrophilic nature, resulting in a staggering 75% of ingested TCs discharged into sewerages through urine and feces in its active form [3]. Unfortunately, the bio-toxicity of TC towards microorganisms nullifies the effectiveness of biological sewage treatments methods to reduce TC concentrations prior to its discharge to the broader environment [1]. Moreover, upon release,

tetracycline is rather recalcitrant towards natural elimination processes due to its stable naphthalene ball structure, resulting in its persistence in the environment for extended periods [4]. Alarming, tetracycline has been detected in rivers, lakes, seawater, groundwater and even drinking water [5], with an extreme case of 110,000 ng L⁻¹ of TC detected in the rivers of Brazil [6]. Lamentably, the long term exposure of TCs has led to chronic toxicity towards non-target organisms, with its ecotoxicity affecting aquatic and terrestrial animals [5]. Furthermore, the proliferation of TCs encourage the development and dissemination of antibiotic resistant bacterial strains [7], leading to various infectious diseases causing serious harms to human health [8]. In light of this, numerous techniques have been devised to remove TCs from water bodies, such as physical adsorption [9], electrochemical oxidation [10] and membrane filtration [11]. However, these technologies suffer from significant drawbacks of high capital intensity and energy requirements.

Photocatalysis offers an alternative solution by tapping into inexhaustible solar energy to degrade emerging pollutants such as tetracycline. Briefly speaking, irradiated light energy is absorbed by the photocatalyst to produce photoexcited electron-hole pairs, which react

* Corresponding author.

E-mail address: chai.siang.piao@monash.edu (S.-P. Chai).

<https://doi.org/10.1016/j.apcatb.2023.122836>

Received 9 March 2023; Received in revised form 25 April 2023; Accepted 1 May 2023

Available online 2 May 2023

0926-3373/© 2023 The Authors. Published by Elsevier B.V. This is an open access article under the CC BY license (<http://creativecommons.org/licenses/by/4.0/>).

with adsorbed water to form reactive oxygen species such as hydroxyl radicals ($\cdot\text{OH}$) and superoxide anion radicals ($\cdot\text{O}_2^-$) that attack and degrade tetracycline molecules into harmless byproducts. Among various photocatalyst options, titanium dioxide (TiO_2) stands out as a prominent candidate for photocatalysis applications due to its strong redox capabilities, remarkable optoelectronic properties, photochemical stability and environmentally benign nature [12,13]. However, poor optical response in the visible light region coupled with rapid recombination of photogenerated charge carriers hampers its practical application. Recently, oxygen vacancy modulation within the TiO_2 crystal lattice has garnered attention to augment its photocatalytic performance [14,15]. Therein, oxygen vacancy engendered mid gap states proved commendatory in modulating the visible light photo-response as well as mediating the enhanced separation and lifetime of photogenerated charge carriers. Nonetheless, further improvement headspace in augmenting charge carrier separation remains untapped and warrants exploration endeavors.

Given that tetracycline pollutants prevail primarily in flowing water bodies, the proposition of harvesting discrete fluid mechanical hydro energy for degradation enhancement is incontestably opportune to tap into stranded energy sources. In that arena, piezophotocatalysis emerged as a promising technology to promote the charge separation of photoexcited electron hole pairs upon subjecting to mechanical stimuli. Succinctly, when an externally applied force deforms a non-centrosymmetric piezo material, a strain-induced piezoelectric polarization field is formed. The piezopotential dipole moments then act as the driving force for the spatially directed charge transport of photogenerated charge carriers towards opposite ends of the piezo-induced electric field, thereby facilitating charge separation suppressing the electron-hole recombination process [16]. As such, piezo-phototronics, an integration of piezoelectricity, photoexcitation and semiconductor properties, have transpired superior synergistic effects for modulating the generation, transport and separation process via the application of external strain [16]. However, an overwhelming majority of piezophotocatalyst necessitates the strong mechanical forces of bubble cavitation under high-frequency ultrasonic conditions to invoke piezopolarization effectively due to their weak piezoelectricity. Ultimately, such intense energy requirement impedes the practicality of large-scale applications.

Potassium sodium niobate (KNN) based perovskites have been extensively investigated as a promising lead-free alternative to the conventional toxic lead zirconate titanate (PZT) ceramics due to its favourable piezoelectricity, excellent ferroelectric properties and high Curie temperature. In particular, various manipulation of KNN's polymorphic phase transition (PPT) boundaries have been undertaken to increase the rhombohedral-orthorhombic transition temperature (T_{R-O}) and decrease the orthorhombic-tetragonal transition temperature (T_{O-T}) close to room temperatures for augmenting its piezoelectricity. In 2014, Zheng et al. modified KNN with Sb, Li and Zr elements to achieve a remarkably high piezoelectric constant (d_{33}) of 490 pC N $^{-1}$, rivalling that of PZT based ceramics. Chiefly, Zr^{4+} and Sb^{5+} increased T_{R-O} , Bi^{3+} , Li^+ and Sb^{5+} decreased T_{O-T} , resulting in the simultaneously compression of orthorhombic zone and formation of a new R-T phase boundary at ambient temperatures ($\sim 30^\circ\text{C}$), substantially enhancing its piezoelectric properties. Despite these advances in the field of piezoelectrics, R-T mixed phase KNN modifications has yet to penetrate the sphere of piezophotocatalysis applications. Moreover, the trade-off relationship between piezoelectrics and photocatalyst has yet to be investigated.

In this work, the cross-pollination of high performance piezoelectrics and high photoresponse photocatalyst were amalgamated for the piezophotocatalytic degradation of tetracycline. Acid treated blue TiO_2 and R-T mixed phase KNN were conjugated via sonochemical electrostatic self-assembly to produce BT-KNN composites. Optoelectronic results indicate an n-n heterojunction band alignment arising from the equilibration of Fermi levels, leading to the formation of built-in electric fields. Piezophotoelectrochemical measurements illustrated a successively augmented photocurrent and decreased charge transfer resistance

with increased agitation. Moreover, the radiative recombination of electron hole pairs were ameliorated by the facilitation of charge separation under piezoelectric polarization field. Furthermore, BT-KNN composites exhibit an improved degradation performance and enhancement in apparent rate constant with increased frequency of fluid disturbances, resulting in 91.3% tetracycline degradation in 3 h under 4 Hz oscillations. Structural deformation of BT-KNN under compressive/tensile strain resulted in spontaneous piezoelectric polarization which modulated the band bending and interfacial charge transfer for enhanced degradation performance. Tradeoff dynamics between the high photoactivity of BT and high piezoelectric enhancement of KNN were explicated, showing a quintessential balance is required for optimal performance. Unlike conventional piezophotocatalyst which require ultrasonic activation, BT-KNN composites exude performance amplification under mild fluid disturbances. Hence, these findings collectively lead piezophotocatalysis a step closer to large-scale commercial applications.

2. Material and methods

2.1. Reagents

Titanium (IV) fluoride (TiF_4), potassium carbonate (K_2CO_3 , $\geq 99\%$), antimony (III) oxide (Sb_2O_3 , 99%), sodium hydroxide (NaOH , $\geq 98\%$), ammonium oxalate (AO, $\geq 99\%$), isopropanol (IPA, $\geq 99.7\%$), ethylenediaminetetraacetic acid disodium salt dihydrate (EDTA-2Na , $\geq 99.0\%$), 1,4-benzoquinone (BQ, $\geq 98\%$) and tetracycline (TC, $\geq 98\%$) were obtained from Sigma Aldrich. Titanium (III) chloride (TiCl_3 , 30% in 10% HCl), zirconium dioxide (ZrO_2 , 99%), polyvinyl alcohol fully hydrolyzed (PVA) were obtained from Merck. Absolute ethanol (EtOH , $\geq 99.9\%$) was obtained from J. T. Baker. Sodium sulfate (Na_2SO_4 , $\geq 99\%$) was obtained from Macron Fine Chemicals. Anhydrous sodium carbonate (Na_2CO_3 , $\geq 99.5\%$) was obtained from RANKEM. Niobium (V) oxide (Nb_2O_5 , $\geq 99.5\%$) and bismuth (III) oxide (Bi_2O_3 , $\geq 99.9\%$) were obtained from Nacalai Tesque. Sulphuric acid (H_2SO_4 , 95–97%) was obtained from Friendemann Schmidt. PELCO® colloidal silver paste was obtained from Ted Pella. All chemicals were used as received without further purification.

2.2. Material synthesis

2.2.1. Blue TiO_2 synthesis

Oxygen-deficient blue TiO_2 was synthesized using the solvothermal method as described in our previous work [14]. Briefly, 2 ml of TiCl_3 solution was added to 5 ml of absolute ethanol containing the suitable amounts of TiF_4 to produce $\text{Ti}^{4+}:\text{Ti}^{3+}$ molar ratios of 0.06. The solution was stirred for 30 min then transferred to a Teflon-lined stainless steel autoclave and heated to 180°C for 24 h under a ramping rate of $10^\circ\text{C min}^{-1}$. The obtained photocatalyst was then washed successively with ethanol, 0.1 M NaOH and DI water.

2.2.2. Acid treatment of blue TiO_2

300 mg of blue TiO_2 was dispersed in 100 ml of H_2SO_4 (95–97%) and stirred for 24 h at 40°C . The suspension was then quenched into 300 ml of DI water under constant stirring in an ice bath. The resulting mixture was centrifuged at 8000 rpm for 10 min and further washed with DI water to remove the acid. The obtained acid treated blue TiO_2 is denoted as BT hereafter.

2.2.3. KNN synthesis

$0.96(\text{K}_{0.48}\text{Na}_{0.52})(\text{Nb}_{0.95}\text{Sb}_{0.05})\text{O}_3-0.04(\text{Bi}_{0.5}(\text{Na}_{0.82}\text{K}_{0.12})_{0.5})\text{ZrO}_3$ was synthesized via conventional solid-state reaction exapted from the previous work [17]. The raw materials K_2CO_3 , Na_2CO_3 , Nb_2O_5 , Sb_2O_3 , Bi_2O_3 and ZrO_2 were stoichiometrically mixed and ground to fine powder. The mixture was then ultrasonicated in absolute ethanol for 3 h and stirred vigorously for 1 h. After filtration and drying, the solids were

calcined at 850 °C for 6 h under a ramping rate of 5 °C min⁻¹. Subsequently, 5 wt% PVA binder solution was added to 340 mg of calcined powder in a 1 wt% PVA to powder ratio and ground to homogeneity. The resultant powders were isostatically pressed under 100 MPa for 5 min to produce pellets of 13 mm diameter and 1 mm thickness. After drying in an oven to remove moisture, the pellets were buried in calcined powder of the same composition (100 mg powder per pellet) prior to sintering to reduce alkali volatilization [18]. The buried pellets were then subjected to 600 °C heating for 1 h at a ramping rate of 2 °C min⁻¹ to incinerate the PVA binder and subsequently raised to 1085 °C for 3 h at a ramping rate of 5 °C min⁻¹ for solid state sintering and densification. The sintered pellets were ground to fine powder and further ultrasonicated in DI water for 3 h and collected via filtration. The obtained powder is hereafter denoted as KNN.

2.2.4. BT-KNN synthesis

BT-KNN conjugated composites were synthesized via sonochemical electrostatic self-assembly. Briefly, KNN was first ultrasonicated in DI water for 10 min before BT was added and subjected to another 10 min ultrasonication to produce composite dispersions of 1 mg ml⁻¹ concentration. The mixture was then stirred vigorously for 2 h to aid the self-assembly process. The collected composites is hereafter denoted as BT-KNN-x, where KNN/BT weight ratio x = 0.8, 1.0, 1.2. Conversely, BT-SiO₂ with a 1.0 weight ratio was synthesized as a control using the same procedure.

2.3. Material characterization

Zeta potential of the materials were scrutinized under Malvern Nano ZS Zetasizer using DTS 1070 folded capillary cell. Crystallographic properties of the materials were examined using X-ray diffractometer (XRD) (Bruker D8 Discover) with scan rate of 2° s⁻¹ using Cu K α radiation (λ = 1.54056 Å). Morphological analysis were performed under Hitachi SU8010 field emission scanning electron microscope (FESEM) at an accelerating voltage of 5 kV. Ultraviolet-visible (UV-vis) diffused reflectance properties of the materials were investigated using Agilent Cary 100 UV-vis spectrophotometer operating from 200 nm to 800 nm with BaSO₄ as the reflectance standard. Piezoresponse force microscopy (PFM) was conducted using Bruker Multimode 8 atomic force microscopy (AFM) with a 3.0 N m⁻¹ spring constant Pt/Ir coated conductive tip over a scan area of 500 nm x 500 nm at 3 V AC drive voltage and 300 kHz drive frequency [19]. Kelvin probe force microscopy (KPFM) were investigated using Bruker Multimode 8 atomic force microscopy (AFM) under ambient conditions with a scan area of 20 μ m x 20 μ m. Prior to analysis, the samples were dispersed in absolute ethanol and spray coated on a fluorine-doped tin oxide (FTO) glass substrate, which were subsequently mounted onto a conductive sample puck with colloidal silver paste for uninterrupted electrical connectivity. Photoluminescence (PL) properties of the composites were analysed under Perkin Elmer LS 55 with an excitation wavelength of 317 nm.

2.4. Piezophotoelectrochemical measurement

Piezophotoelectrochemical (PPEC) measurements were probed using Metrohm Autolab PGSTAT128N workstation annexed to a conventional three-electrode cell with Pt rod as the counter electrode, Ag/AgCl saturated with 3 M KCl solution as the reference electrode and 0.5 M Na₂SO₄ as the electrolyte. The working electrode with an active area of 1 cm² was fabricated by drop coating the piezophotocatalyst-absolute ethanol suspension onto fluorine-doped tin oxide (FTO) glass substrate. 500 W Xenon lamp (CHF-XM-500 W) provided the required illumination whereas IKA RW 20 Digital agitator equipped with 40 mm dia. PTFE paddle blade impeller was employed to induce cross-flow fluid mechanical disturbances.

2.5. Piezophotocatalytic tetracycline degradation

Piezophotocatalytic performance of the composites was investigated via the degradation of tetracycline. Briefly, 10 mg of the piezophotocatalyst was added to 75 ml of 10 ppm tetracycline solution and left in the dark for 30 min to achieve adsorption-desorption equilibrium. Subsequently, the mixture was irradiated with 250 W m⁻² intensity light illumination provided by 500 W Xenon lamp (CHF-XM-500 W) equipped with AM 1.5 light filter for a duration of 3 h. Oscillatory hydrodynamic disturbances were induced via a linear actuator coupled to an impeller with a triangular profile and a pitch of 36.9° at frequencies mimicking fluid disturbances occurring in nature [20]. 3 ml aliquots were sampled every 30 min and centrifuged to remove the piezophotocatalyst traces. The tetracycline concentration was then measured by the absorbance of 357 nm characteristic tetracycline peak via a UV vis spectrophotometer. Tetracycline degradation efficiency was then computed according to Eq. (1). Additionally, tetracycline degradation kinetics were fitted with the pseudo-first-order Langmuir-Hinshelwood equation according to Eq. (2).

$$\eta = \frac{C_o - C}{C_o} \times 100\% \quad (1)$$

$$\ln(C_o/C) = k_{app}t \quad (2)$$

where C_o and C are the tetracycline concentrations before and after piezophotocatalytic degradation respectively, k_{app} is the apparent tetracycline degradation rate constant and t is the duration of piezophotocatalytic degradation.

Scavenger experiments were performed using isopropanol (IPA), ammonium oxalate (AO), ethylenediaminetetraacetic acid disodium salt dihydrate (EDTA-2Na) and 1,4-benzoquinone (BQ) as scavenging agents to capture hydroxyl radicals (\cdot OH), holes (h^+), electrons (e^-) and superoxide radicals (\cdot O₂).

3. Results and discussion

3.1. Sonochemical electrostatic self-assembly

Electrostatic properties of the photocatalytic and piezoelectric constituents were investigated via zeta potential measurements. From Fig. 1a, zeta potential of both pristine blue TiO₂ and KNN lie in the deeply negative territory, implying an inability of self-assembly due to electrostatic Coulomb repulsion. Upon acid treatment of blue TiO₂, the zeta potential of the resultant BT sample inverted into the positive region, affording the conjugation of BT and KNN samples via sonochemical electrostatic self-assembly. In the same vein, BT-SiO₂ composites were similarly synthesized as the control sample (Fig. S1).

3.2. Structural and morphological properties

The crystallographic properties of the as-synthesized materials were evaluated using XRD characterization. From Fig. 1b, diffraction peaks of BT match well with the anatase phase of TiO₂, indicating that acid treatment did not alter the structural properties of blue TiO₂ photocatalyst. Moreover, XRD spectra of KNN exhibit perovskite structure characteristics, indicating the formation of a stable solid solution. Additionally, diffraction peaks of BT-KNN composites indexed well to the spectral combination of BT and KNN constituents as expected. Close scrutiny of KNN XRD spectra in the 44–47° 2 θ range reveals a multi-phase coexistence within the KNN structure (Fig. 1c). Furthermore, Rietveld refinement of the observed XRD spectra was well-fitted with rhombohedral ($R3m$ space group) and tetragonal ($P4mm$ space group) symmetries, confirming the R-T two-phase coexistence within KNN (Table S1). FESEM images depict the morphology of BT, which had a particle size ca. 40 nm (Fig. 1d). Conversely, KNN possess an irregular

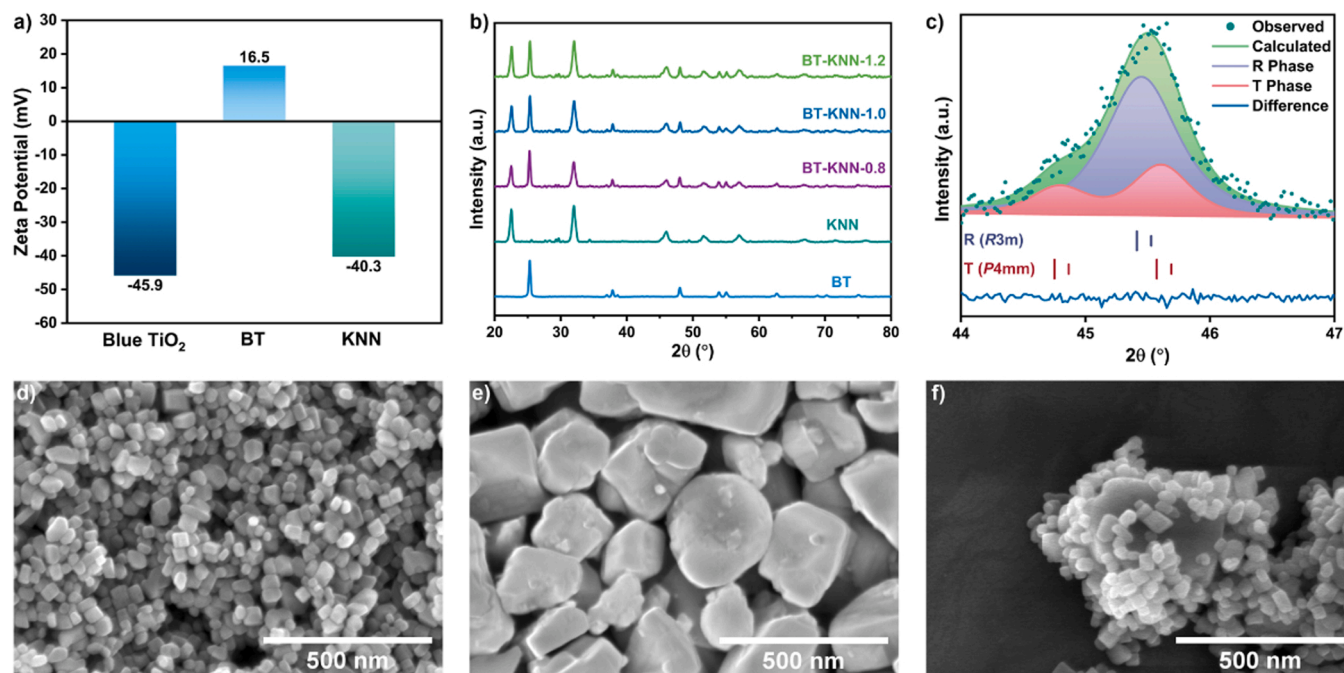


Fig. 1. a) Zeta potentials of blue TiO_2 , BT and KNN in aqueous solvent. b) XRD patterns of the as-synthesized materials. c) Rietveld refinement of KNN XRD spectra along with Bragg positions of R and T phases. FESEM images of d) BT, e) KNN, f) BT-KNN-1.0.

morphology with a particle size of ca. 300 nm (Fig. 1e). In addition, FESEM images of BT-KNN-1.0 illustrate that BT nanoparticles are well decorated onto the surface of KNN, corroborating the electrostatic conjugation of BT and KNN.

3.3. Piezoelectric properties

Piezoresponse force microscopy (PFM) measurements were performed to gain insight into the piezoelectric properties of KNN. Fig. 2a, b

and c illustrate the topography, amplitude and phase images of KNN, respectively. Therein, the piezoelectric amplitude domains corresponded well to the phase images, instantiating the piezoelectric effect in KNN samples. Moreover, butterfly amplitude loops show a characteristic response of piezoelectric materials, highlighting the distinct piezoelectric polarization switching behaviour of KNN (Fig. 2d) with a piezoelectric coefficient of $d_{33} = 298 \text{ pm V}^{-1}$ (Eq. S1). In addition, square phase hysteresis loops of KNN depicts a near 180° phase reversal upon voltage sweeping between $+12 \text{ V}$ and -12 V (Fig. 2e), indicating

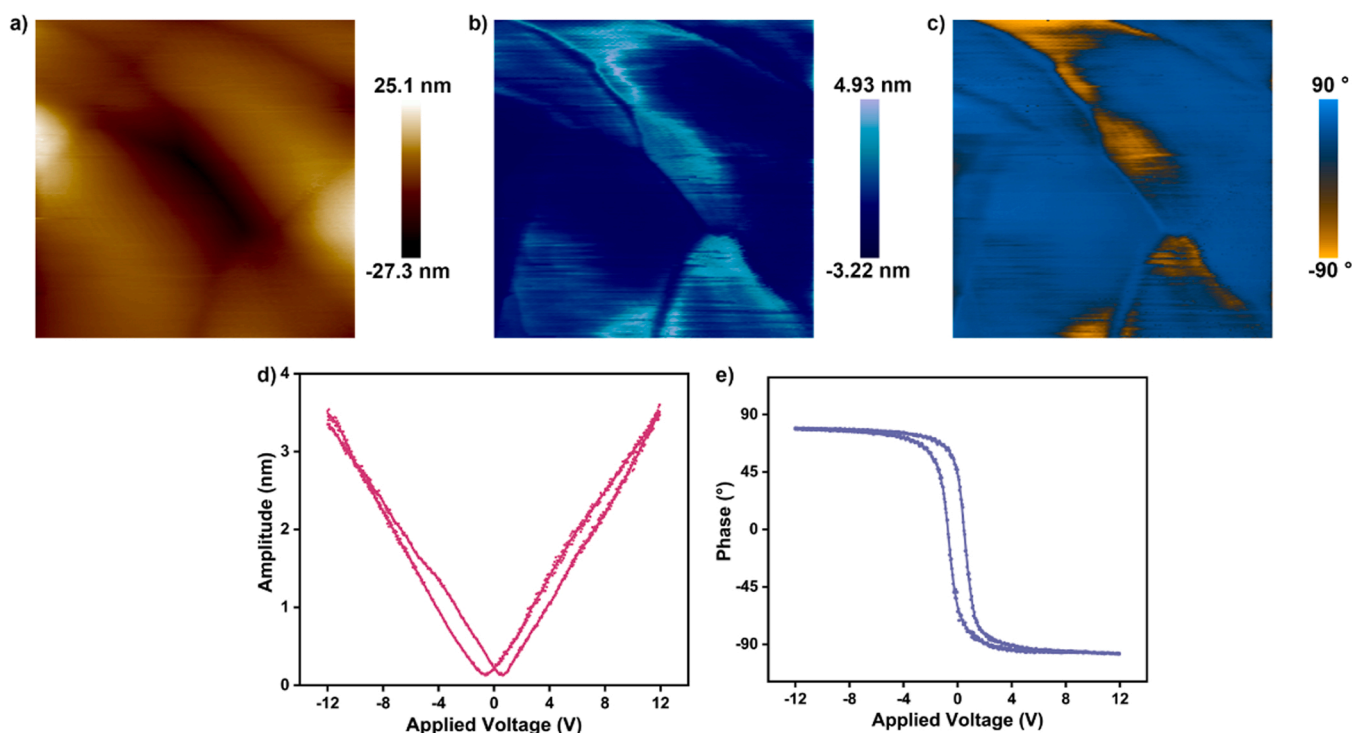


Fig. 2. a) Topography, b) amplitude, c) phase images, d) butterfly loops and e) hysteresis loops of KNN.

the existence of 180° piezoelectric domains. Granted, the ease of phase reversal observed arises from the beneficial multiphase coexistence which enhances polarization rotation [21]. Hence, these results substantiate the superior piezoelectric properties of R-T mixed phase KNN.

3.4. Optoelectronic properties

DRS spectra of BT and KNN depicted strong optical response in the UV region with an absorption edge wavelength of ca. 390 nm and 394 nm respectively as a result of electronic band-to-band transitions as shown in Fig. 3a. Moreover, BT exhibited an absorption tail in the visible and NIR region arising from the presence of mid gap states ca. 1 eV below the conduction band [14]. Besides, Tauc plot of Kubelka-Munk (KM) function delineates the band gap (E_g) of BT and KNN to be 3.18 eV and 3.15 eV respectively (Fig. 3b). Mott-Schottky (M-S) analysis gleans further insights into the flat band potentials of BT and KNN samples as illustrated in Fig. 3c and d. Chiefly, both BT and KNN exhibit a positive Mott-Schottky slope, signifying n-type semiconductor characteristics. Converting the flat band potentials from Ag/AgCl to normal hydrogen electrode (NHE) potentials [22], the conduction band potentials (E_{CB}) of BT and KNN were computed to be -0.50 V and -0.28 V respectively. Conversely, the valence band potentials (E_{VB}) of BT and KNN were calculated to be 2.68 V and 2.87 V respectively via the formula $E_g = E_{VB} - E_{CB}$.

To elucidate the charge transfer mechanism between BT and KNN, the contact potential difference (CPD) of the samples were measured under Kelvin probe force microscopy (KPFM). The samples were spray coated such that the sample-FTO boundary was well preserved (Fig. S2). Subsequently, surface potential mapping scans were performed by

sweeping across the sample-FTO boundary. As the analysis was performed under ambient conditions, FTO was employed as a common reference to determine the relative work functions between BT and KNN samples [23]. From Fig. 4a and b, the topography and the surface potential maps of BT and KNN show distinct boundary between samples and FTO. Moreover, consistency between boundary of height transition and potential profile transition was observed, indicating a clean KPFM measurement. Two-dimensional potential maps of BT and KNN further depicts a clear boundary between samples and FTO (Fig. 4c and d). Thereafter, the contact potential difference voltage (ΔV_{CPD}) between the samples and FTO were computed using histogram analysis, and ΔV_{CPD} for BT and KNN were determined to be $+154$ mV and -129 mV respectively with reference to FTO (Fig. 4e and f). As such, BT exhibits a higher Fermi level as compared to KNN.

Considering the band potentials and contact potential difference, the band alignment between BT and KNN can be explicated. Fig. 5a and b shows the band alignment and relative fermi levels of BT and KNN before conjugation. Upon electrical contact, the difference in Fermi level causes electron migration from BT to KNN, resulting in the upward band bending of BT and downward band bending of KNN, forming a built-in electric field at the BT-KNN interface. Given that the magnitude of Fermi level difference ($\Delta E_{F, BT-KNN} = 283$ mV) exceeds the difference in conduction band potentials ($\Delta E_{CB, BT-KNN} = 220$ mV), an n-n heterojunction band alignment is formed in BT-KNN composites (Fig. 5c).

3.5. Piezophotoelectrochemical characterization

Photoelectrochemical (PEC) measurements were also examined to provide insights into the charge transfer characteristics of the

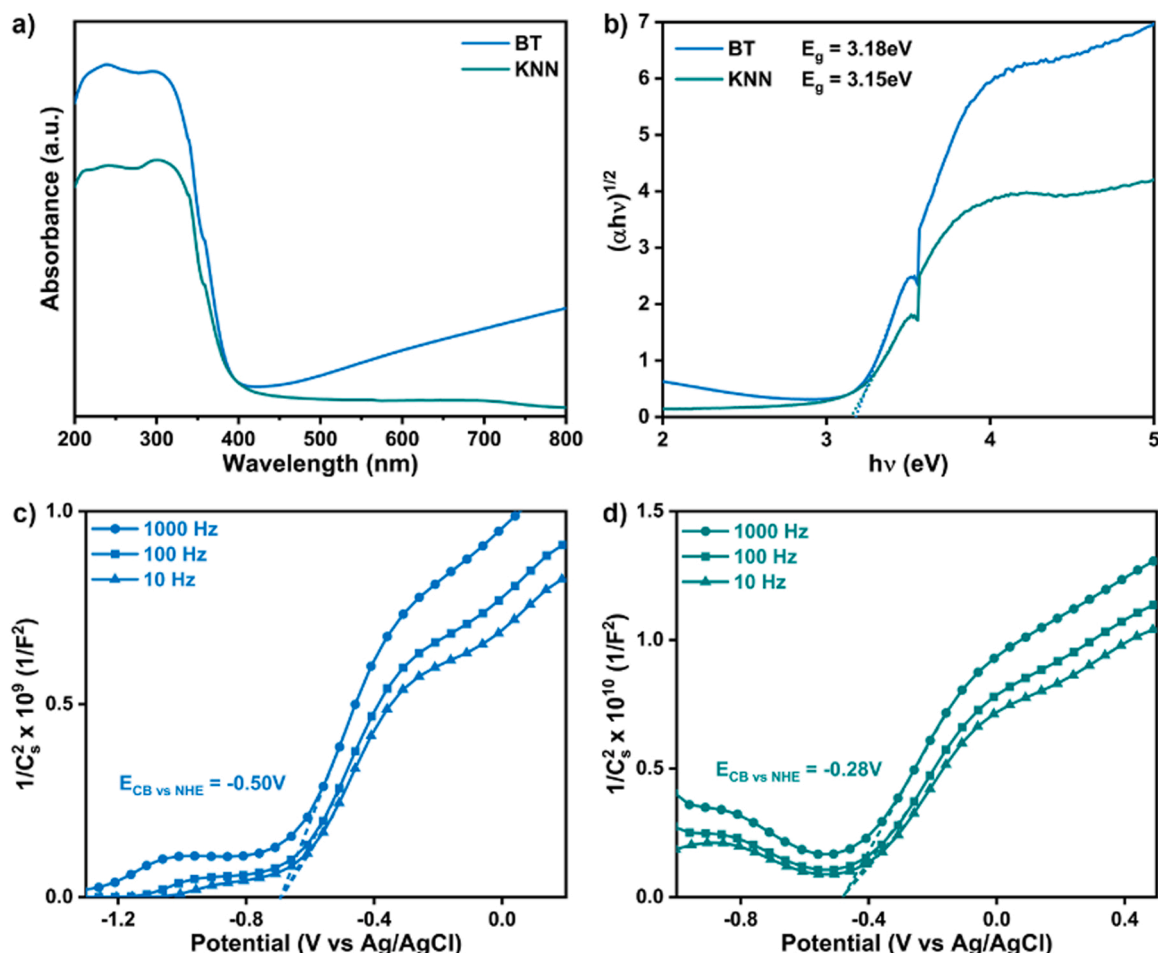


Fig. 3. a) UV-vis DRS spectra and b) Tauc plot of BT and KNN. Mott-Schottky plots of c) BT and d) KNN.

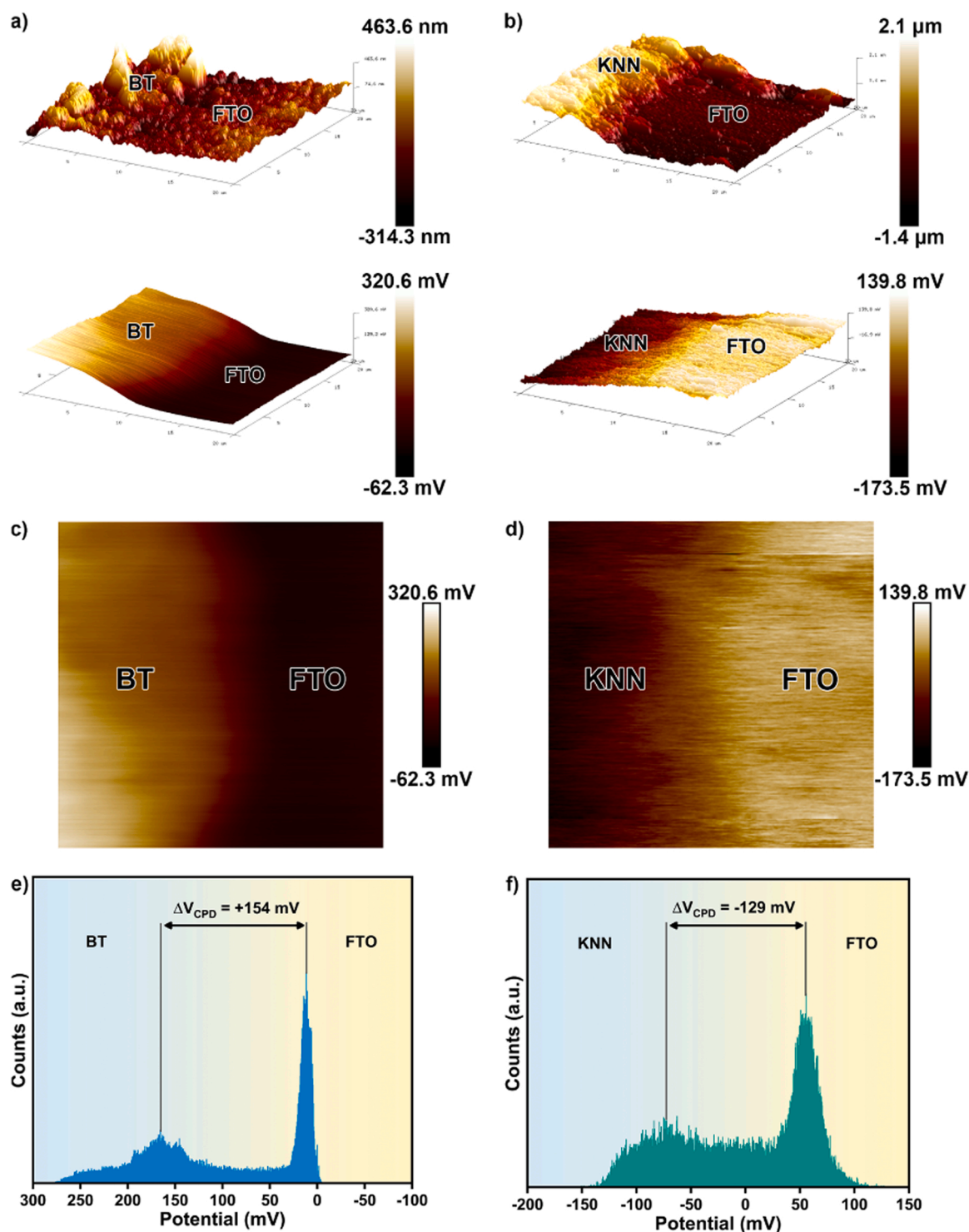


Fig. 4. Topography and surface potential maps of a) BT and b) KNN. 2D potential maps of c) BT and d) KNN respectively. KPFM histogram analysis of e) BT and f) KNN respectively.

composites. Herein, BT-SiO₂ composite devoid of heterojunction advantages and piezoelectric properties was employed as a control specimen. From Fig. 6a, BT-KNN composites exhibit a significantly enhanced photocurrent under stagnant conditions as compared to BT-SiO₂, with BT-KNN-1.0 showing the highest photocurrent density. Chiefly, the phototronic contributions of KNN alone cannot sufficiently elucidate the markedly augmented photocurrent due to its low photocurrent magnitude (Fig. S3). Admittedly, the photocurrent enhancement can be mainly attributed to the advantageous heterojunction coupling of BT and KNN,

which precipitates a propitious interfacial electronic charge transfer due to the built-in electric field at the junction interface.

Furthermore, the composites were subjected to intermittent light on and off cycles under agitation to interrogate the piezo-phototronic enhancement effect. From Fig. 6b, BT-KNN composites illustrated a successively higher photocurrent with increased agitation intensity. Principally, improvements due to increased mass transfer can be excluded from the plausible explanations, as BT-SiO₂ did not exhibit any notable photocurrent increase with increasing agitation. Moreover, as

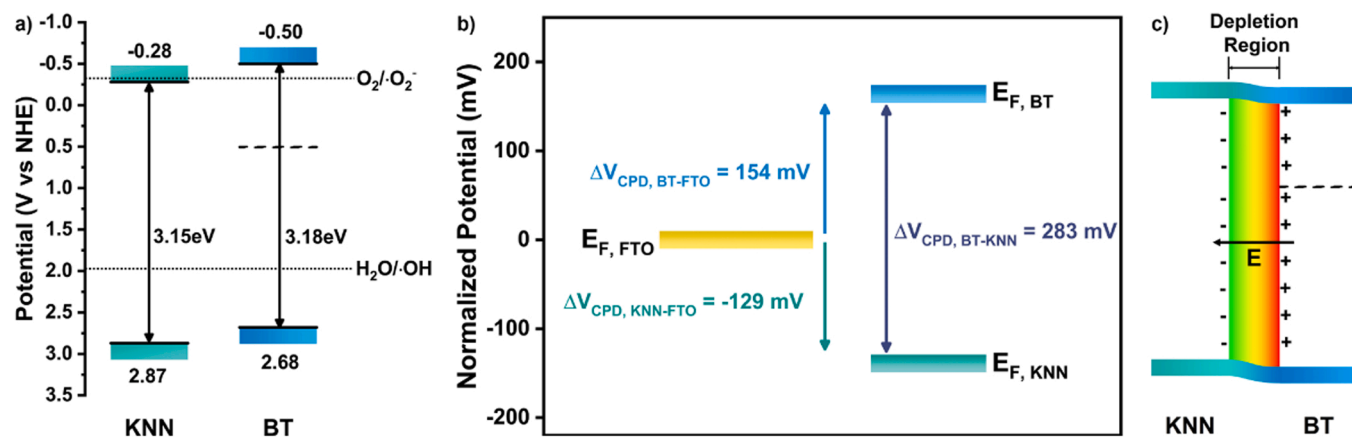


Fig. 5. a) Band alignment and b) relative fermi levels of BT and KNN before conjugation. c) Electronic band diagram of BT and KNN after contact.

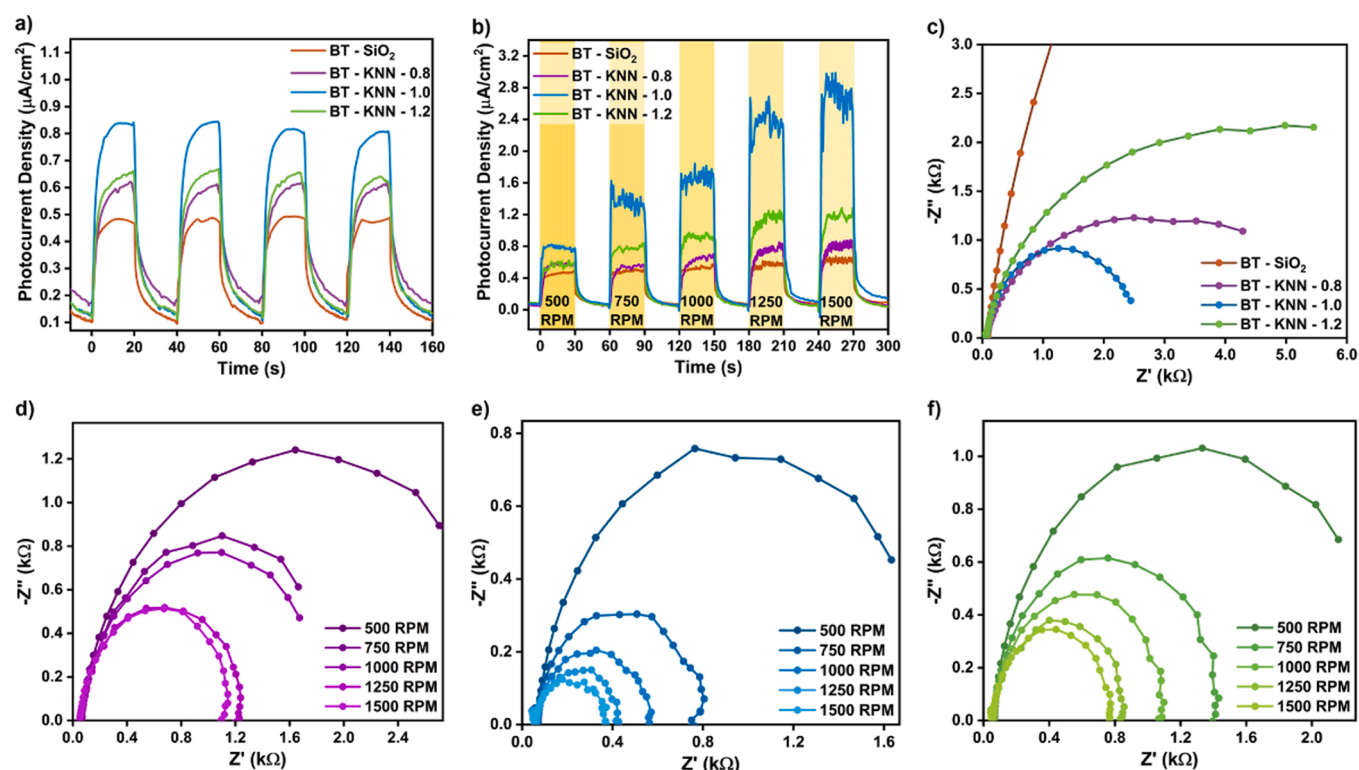


Fig. 6. Photocurrent spectra of the as-synthesized composites under intermittent light on light off cycles a) without and b) with agitation. c) Nyquist plots of the as-synthesized composites. Nyquist plots of d) BT-KNN-0.8, e) BT-KNN-1.0 and f) BT-KNN-1.2 under agitation.

BT-KNN-1.0 composite did not show noteworthy directional current under dark conditions (Fig. S4), piezotronic current can be considered inconsequential and light irradiation is the key activation required. Thus, the photocurrent enhancement can only be attributed to the piezophototronic effect, in which spontaneous piezoelectric polarization under agitation conditions promoted the efficacious BT-KNN interfacial charge separation. In other words, this corroborates the triality of BT-KNN semiconductor composites endowed with photoactivity in addition to its piezoelectric properties, i.e. the three-way piezo-phototronic coupling modality.

Nyquist analysis of the composites divulged that BT-KNN-1.0 possess the smallest Nyquist semi-circular arc radius among all samples (Fig. 6c), indicating it possess the lowest charge transfer impedance. Additionally, BT-KNN samples exhibited a distinctively diminished Nyquist arc radius upon the introduction of agitation (Fig. 6d-f),

whereas BT-SiO₂ did not show any appreciable changes (Fig. S5). Ostensibly, this illustrates the effect of piezoelectric polarization in modulating the charge transfer resistance to accelerate the interfacial charge transfer process.

3.6. Piezophotoluminescence characterization

Conventional photoluminescence (PL) analysis of the composites under stagnant conditions exemplify the reduced PL peak intensities of BT-KNN as compared to BT-SiO₂, with BT-KNN-1.0 exhibiting the lowest PL peak intensity (Fig. 7a). Principally, the built in electric field afforded by the coupling of BT-KNN enhanced the effective separation of photogenerated charged carriers and impede the rapid recombination of photoexcited electron-hole pairs. The piezophotoluminescence (PPL) characteristics were also investigated by subjecting the composites to in-

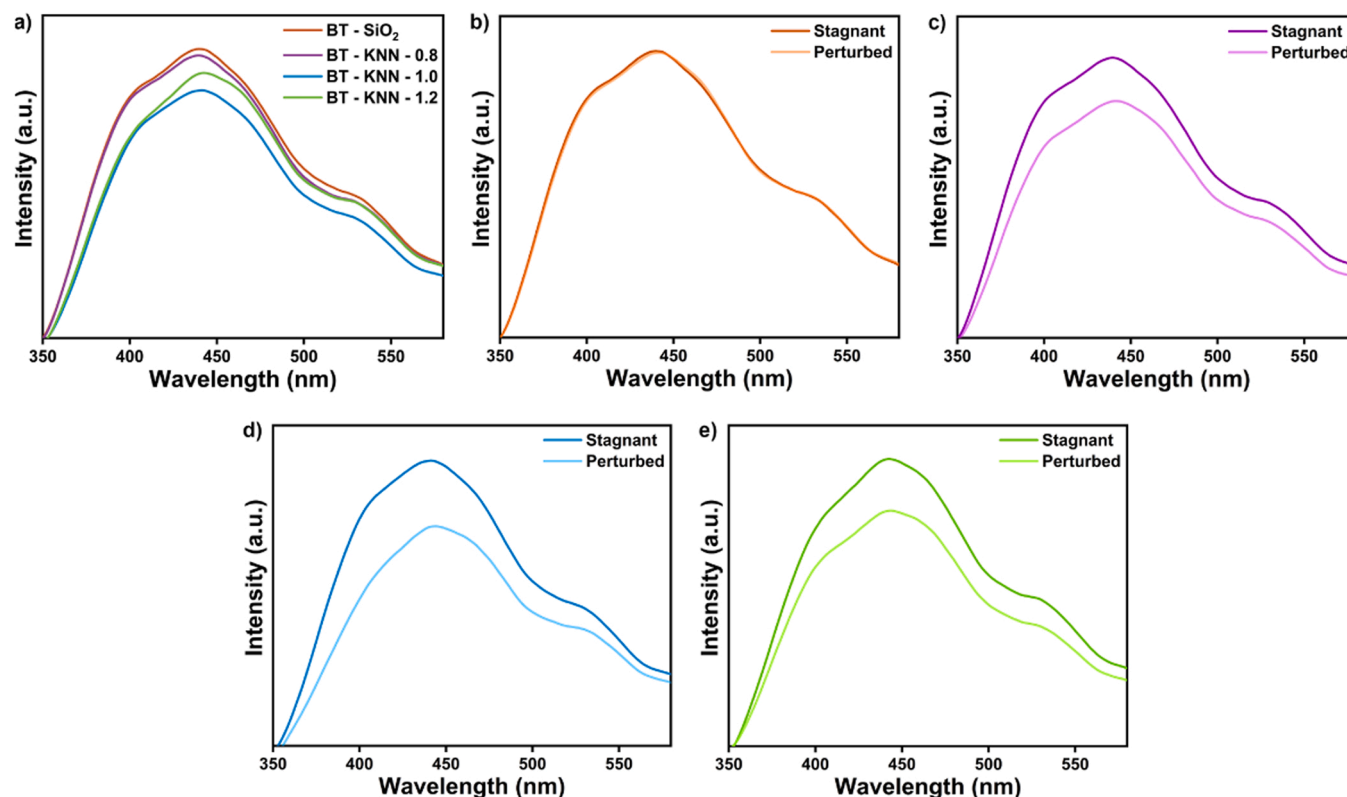


Fig. 7. a) Photoluminescence (PL) spectra of the as-synthesized composites. Piezophotoluminescence (PPL) spectra comparison of b) BT-SiO₂, c) BT-KNN-0.8, d) BT-KNN-1.0 and e) BT-KNN-1.2 under stagnant and perturbed conditions.

situ perturbation via mechanical means. From Fig. 7b, BT-SiO₂ showed no noticeable change in PPL peak intensities. On the other hand, a quenching effect of the PPL peak was observed for BT-KNN samples upon vigorous perturbation (Fig. 7c, d and e). Ostensibly, the invoked piezo-phototronic effect ameliorated the radiative recombination of electron hole pairs by facilitating the separation of photogenerated charge carriers under the piezoelectric polarization field.

3.7. Piezophotocatalytic tetracycline degradation

Tetracycline degradation under simulated solar irradiation without external disturbances was employed to first evaluate photocatalytic performance of the as-synthesized composites, with the corresponding concentration curves depicted in Fig. 8a. Gratifyingly, all BT-KNN samples exhibited superior degradation efficiencies over the BT-SiO₂ control sample, with BT-KNN-1.0 taking the lead. Moreover, pseudo-first-order kinetic model fitting of the degradation curves was performed to assess the apparent rate constant of the degradation. From Fig. 8b, BT-KNN-1.0 professed the highest apparent rate constant among all samples, which is in concordance with the characterization results observed *a priori*. Indeed, BT-KNN-1.0 composite showed 83.6% degradation of tetracycline after 3 h of illumination, whereas BT-SiO₂, BT-KNN-0.8 and BT-KNN-1.2 only achieved 69.2%, 82.2%, 76.6% degradation efficiencies respectively (Fig. 8c). Hence, the optimal coupling of BT and KNN is imperative to ameliorate the electronic charge transfer and actualize its superior degradation performance.

The piezophotocatalytic degradation performance of the composites were then further interrogated by inducing gentle oscillatory hydrodynamic disturbances as shown in Fig. 8d. From Fig. 8f, g and h, BT-KNN composites revealed an increasing degradation performance with increased frequency of disturbances. Conversely, BT-SiO₂ showed only slight response to the disturbances due to minor mass transfer improvements (Fig. 8e). Kinetic relation curves of BT-KNN samples also

demonstrated the favourable increase in apparent rate constant with increased oscillation frequency (Fig. 8j, k, and l) (Table S2), whereas BT-SiO₂ only had a meagre change in apparent rate constant (Fig. 8i). Moreover, BT-KNN-1.0 professed a spectacular 91.3% tetracycline degradation in 3 h under 4 Hz oscillations, exhibiting an impressive performance enhancement under such mild oscillations (Fig. 8m). As such, this testifies the role of the advantageous piezo-phototronic effect in amplifying its degradation performance.

Close scrutiny of the degradation performance unveils interesting dynamics between the contributions of BT and KNN within the composites. Upon normalizing the degradation performances of the composites to 0 Hz, comparisons of piezo-phototronic enhancements of KNN within the composites can be observed. From Fig. 8n, the amount of piezophotocatalytic enhancement is directly correlated to the amount of KNN present within the composite, with BT-KNN-1.2 demonstrating the highest performance augmentation. However, its nominal degradation performance under 4 Hz (89.9%) is still second fiddle to that of BT-KNN-1.0 (91.3%). Granted, BT-KNN-1.2 faces a shortfall in BT composition, which primarily contributes photoactivity to the composites (*vide supra*). In other words, BT-KNN-1.2 experiences great piezoelectric polarization from KNN abundance, but at the detriment of photoactivity due to BT deficiency. Therein, BT and KNN serves a complimentary role within BT-KNN composites, with BT bestowing the bulk of photoactivity whereas KNN imparts the piezo-phototronic enhancements. As such, BT-KNN-1.0 delicately balances the complementary tradeoff relationship in an optimal conjugation of BT and KNN, delivering the highest piezophotocatalytic performance.

Cyclic stability of BT-KNN-1.0 piezophotocatalyst were also examined under 3 consecutive cycles. From Fig. 9a, BT-KNN-1.0 illustrates modest piezophotocatalytic stability, retaining 89% degradation performance under repeated utilization. Control experiments were also performed on BT-KNN-1.0 to disambiguate piezophotocatalytic degradation from other contributions. Ostensibly, piezophotocatalysis

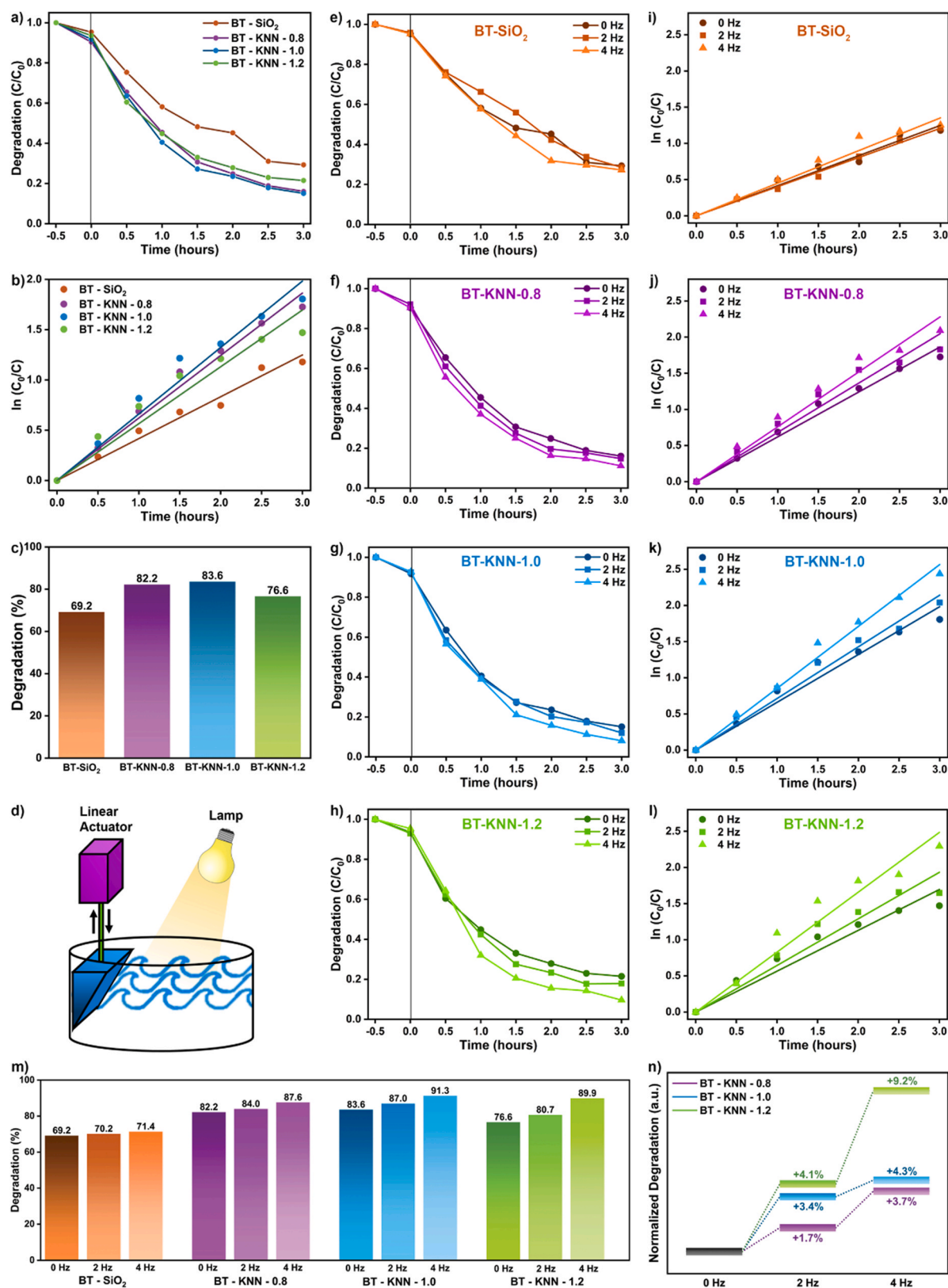


Fig. 8. a) Photocatalytic tetracycline degradation curves, b) pseudo-first-order kinetic model fitting and c) degradation efficiencies of the as-synthesized composites. d) Experimental setup of piezophotocatalytic tetracycline degradation. Piezophotocatalytic tetracycline degradation curves of e) BT-SiO₂, f) BT-KNN-0.8, g) BT-KNN-1.0 and h) BT-KNN-1.2 under oscillatory hydrodynamic disturbances. Pseudo-first-order kinetic model fitting of i) BT-SiO₂, j) BT-KNN-0.8, k) BT-KNN-1.0 and l) BT-KNN-1.2 under oscillatory hydrodynamic disturbances. m) Summary of piezophotocatalytic degradation efficiencies. n) Normalized degradation efficiencies of BT-KNN composites.

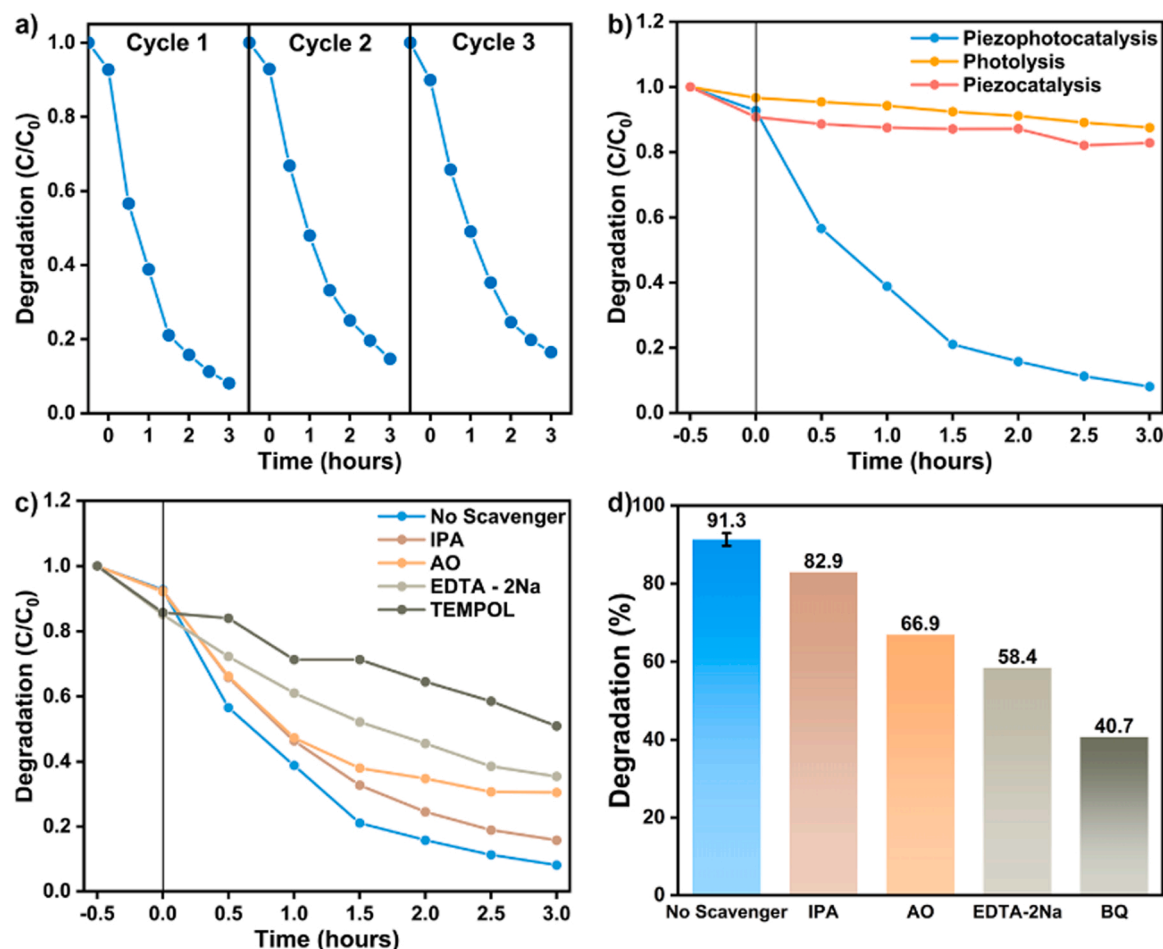


Fig. 9. a) Piezophotocatalytic stability test of BT-KNN-1.0. b) Photolysis and piezocatalysis control experiments comparison of BT-KNN-1.0. c) Piezophotocatalytic degradation curves and d) degradation efficiencies of BT-KNN-1.0 in the presence of IPA, AO, EDTA-2Na and BQ scavengers.

performance starkly outmatched the control experiments, negating photolysis and piezophotocatalysis effects (Fig. 9b). Scavenger experiments were conducted to identify the main reactive oxygen species (ROS) responsible for tetracycline degradation, in which the reactant medium were spiked with isopropanol (IPA), ammonium oxalate (AO), disodium EDTA (EDTA-2Na) and 1,4-benzoquinone (BQ) to scavenge hydroxyl radicals ($\cdot\text{OH}$), holes (h^+), electrons (e^-) and superoxide radicals ($\cdot\text{O}_2^-$) respectively. From Fig. 9c and d, IPA, AO and EDTA-2Na diminished the degradation efficiency by 8.4%, 24.4% and 32.9% respectively, indicating that hydroxyl radicals, holes and electrons evince a weak effect on degradation performance. Conversely, BQ impeded the degradation efficiency by 50.6%, signifying that tetracycline degradation is predominantly affected by superoxide anion radicals.

3.8. Piezophotocatalytic degradation mechanism

Taking into consideration the results thus far, the piezophotocatalytic degradation mechanism can be elucidated. Upon light illumination, electrons are photoexcited from VB to CB of both BT and KNN, with major photoactivity contributions from BT and minor involvement from KNN. Due to the built-in electric field at the BT-KNN interface and the n-n heterojunction band alignment, electrons in CB of KNN are shuttled towards CB of BT, whereas holes in VB of BT migrate laterally towards VB of KNN. Subsequently, electrons and holes react with adsorbed water molecules to form ROS such as hydroxyl radicals ($\cdot\text{OH}$) and superoxide anion radicals ($\cdot\text{O}_2^-$). The tetracycline molecule is then attacked primarily by superoxide anion radicals and resulting in its degradation

(Fig. 10a).

With the introduction of gentle oscillatory hydrodynamic disturbances, tensile and compressive stress is applied onto the BT-KNN conjugated composite, which causes structural deformation and the generation of a strain-induced piezoelectric polarization field. With reference to Fig. 10b, a tensile strain onto the BT-KNN composite enacts a negative and positive piezopotential on the right and left junction interface respectively [16]. On the left junction interface, an intensified downward band bending occurs, shifting the depletion zone towards BT, leading to enhanced interfacial charge migration between BT and KNN. Conversely, the right junction interface experiences increased upward band bending and shifting of depletion zone towards KNN, obstructing the charge transfer. On the other hand, compressive strain onto the BT-KNN composite imposes a positive and negative piezopotential on the right and left junction interface respectively. Similarly, the right junction undergo enhanced downward band bending and the shifting of depletion zone towards BT, augmenting the advantageous interfacial charge transport. Inversely, the left junction experiences increased upward band bending and shifting of depletion zone towards KNN, occluding the charge migration [16]. Hence, these mechanical induced piezoelectric dipole moments causes the spatially directed charge transport of photogenerated charge carriers towards opposite ends of the piezopolarization field, thereby modulating the charge migration behaviour and suppressing the electron-hole recombination process, enhancing the tetracycline degradation performance.

The trade-off dynamics between BT and KNN is further illustrated in Fig. 10c. With an abundance of BT, a pronounced photoactivity and bountiful catalytic active sites can be realized. However, this occurs at

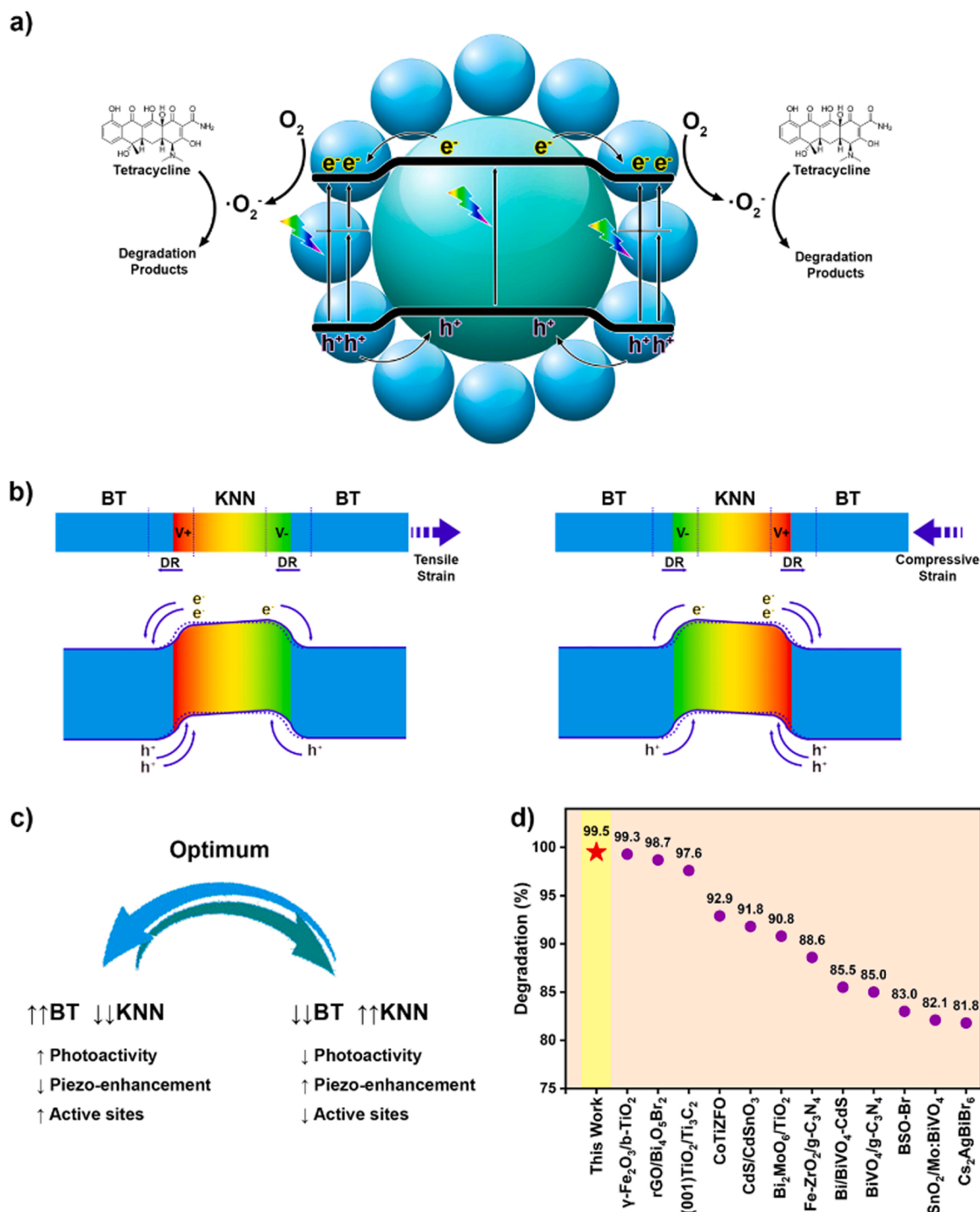


Fig. 10. a) Tetracycline degradation mechanism. Blue and turquoise indicates BT and KNN respectively. b) Piezophotocatalytic charge transport behavior of BT-KNN under tensile and compressive strain. c) Trade-off dynamics between BT and KNN. d) Comparative tetracycline degradation performance of various photocatalyst under simulated solar irradiation.

the impairment of piezoelectric enhancement from KNN deficiency. On the other hand, excessive amounts of KNN results in greater piezoelectric enhancement, but at the detriment of diminished photoactivity and scarce catalytic active sites. Hence, the quintessential balance of BT and KNN constituents is pivotal to achieve optimal piezophotocatalytic performance. Additionally, BT-KNN composites was investigated under simulated solar irradiation at 1 sun intensity to provide a comparative perspective on its tetracycline degradation performance (Fig. S6). Gratifyingly, BT-KNN composites manifests itself in the upper echelon of degradation efficiency benchmarks, testifying its superior performance

for degradation of tetracycline pollutants (Fig. 10d, Table S3).

Crucially, the BT-KNN composites exhibit degradation performance intensification under mild fluid disturbance. This is in contrast to previous reports of piezophotocatalyst, which requires high intensity ultrasonic activation for performance improvement. Granted, this is due to the high mechanical sensitivity derived from the strong piezoelectric behaviour of the R-T mixed phase KNN. As such, this work opens up future avenues for piezophotocatalyst exploration which does not require additional energy input but utilizes fluid mechanical energies already present in typical photocatalytic setups for performance

augmentation.

4. Conclusion

In conclusion, the conjugation of BT and KNN results in an n-n heterojunction formation with built-in electric fields due to the equilibration of Fermi levels. Piezophotocatalytic investigation shows an enhanced photocurrent and diminished charge transfer resistance with increased agitation. Furthermore, piezoelectric polarization field decreased the radiative electron hole pair recombination by modulating the charge separation. Tetracycline degradation performance and apparent rate constant of BT-KNN composites were demonstrated to increase with intensified fluid disturbances, with 91.3% degradation in 3 h under 4 Hz oscillations. Chiefly, the spontaneous piezoelectric polarization arising from hydrodynamic disturbances regulate the interfacial band bending and ameliorating the charge transport. Optimization studies demonstrate the tradeoff dynamics between high photoactivity of BT and high piezo-enhancement of KNN, with BT-KNN-1.0 exhibiting an optimal balance. In contrast to conventional piezophotocatalyst that require ultrasonic activation, BT-KNN composites show performance improvements under mild fluid disturbances. As such, the impact of this work provides inspiration for rich material investigations in the relevant fields of piezophotocatalytic water remediation.

CrediT authorship contribution statement

Yong Jieh Lee: Conceptualization, Methodology, Formal analysis, Investigation, Visualization, Writing – original draft. **Wei-Kean Chong:** Writing – review & editing. **Lutfi Kunianditia Putri:** Writing – review & editing. **Boon-Junn Ng:** Writing – review & editing. **Lling-Lling Tan:** Writing – review & editing. **Ta Yeong Wu:** Writing – review & editing. **Siang-Piao Chai:** Resources, Writing – review & editing, Supervision, Funding acquisition.

Declaration of Competing Interest

The authors declare that they have no known competing financial interests or personal relationships that could have appeared to influence the work reported in this paper.

Data Availability

Data will be made available on request.

Acknowledgements

This work was financially supported by the Monash University Malaysia under the MUM-ASEAN Research Grant Scheme (Ref. No.: ASE-000010).

Supplementary material

Supporting Information Available. Zeta potentials of constituents in control sample. Photograph of sample preparation for KFPM measurements. Photocurrent and Nyquist plots of control sample. Crystal structure parameters of Rietveld refinement. Tetracycline degradation apparent rate constants. Comparative degradation efficiencies under simulated solar irradiation.

Appendix A. Supporting information

Supplementary data associated with this article can be found in the online version at doi:10.1016/j.apcatb.2023.122836.

References

- [1] R. Daghrir, P. Drogui, Tetracycline antibiotics in the environment: a review, *Environ. Chem. Lett.* 11 (2013) 209–227.
- [2] Y. Dai, M. Liu, J. Li, S. Yang, Y. Sun, Q. Sun, W. Wang, L. Lu, K. Zhang, J. Xu, W. Zheng, Z. Hu, Y. Yang, Y. Gao, Z. Liu, A review on pollution situation and treatment methods of tetracycline in groundwater, *Sep. Sci. Technol.* 55 (2020) 1005–1021.
- [3] K.N. Agwuh, A. MacGowan, Pharmacokinetics and pharmacodynamics of the tetracyclines including glycylcyclines, *J. Antimicrob. Chemother.* 58 (2006) 256–265.
- [4] X. He, T. Kai, P. Ding, Heterojunction photocatalysts for degradation of the tetracycline antibiotic: a review, *Environ. Chem. Lett.* 19 (2021) 4563–4601.
- [5] L. Xu, H. Zhang, P. Xiong, Q. Zhu, C. Liao, G. Jiang, Occurrence, fate, and risk assessment of typical tetracycline antibiotics in the aquatic environment: A review, *Sci. Total Environ.* 753 (2021), 141975.
- [6] A.A. Borghi, M.S.A. Palma, Tetracycline: production, waste treatment and environmental impact assessment, *Braz. J. Pharm. Sci.* 50 (2014) 25–40.
- [7] I. Levin-Reisman, I. Ronin, O. Gefen, I. Braniss, N. Shores, N.Q. Balaban, Antibiotic tolerance facilitates the evolution of resistance, *Science* 355 (2017) 826–830.
- [8] S.A. Kraemer, A. Ramachandran, G.G. Perron, Antibiotic pollution in the environment: from microbial ecology to public policy, *Microorganisms* 7 (2019) 180.
- [9] M.B. Ahmed, J.L. Zhou, H.H. Ngo, W. Guo, Adsorptive removal of antibiotics from water and wastewater: Progress and challenges, *Sci. Total Environ.* 532 (2015) 112–126.
- [10] H. Kadji, I. Yahiaoui, Z. Garti, A. Amrane, F. Aissani-Beissad, Kinetic degradation of amoxicillin by using the electro-Fenton process in the presence of a graphite rods from used batteries, *Chin. J. Chem. Eng.* 32 (2021) 183–190.
- [11] Q. Xiang, Y. Nomura, S. Fukahori, T. Mizuno, H. Tanaka, T. Fujiwara, Innovative treatment of organic contaminants in reverse osmosis concentrate from water reuse: a mini review, *Curr. Pollut. Rep.* 5 (2019) 294–307.
- [12] K.L. Schulte, P.A. DeSario, K.A. Gray, Effect of crystal phase composition on the reductive and oxidative abilities of TiO₂ nanotubes under UV and visible light, *Appl. Catal. B* 97 (2010) 354–360.
- [13] L. Sun, Z. Zhao, Y. Zhou, L. Liu, Anatase TiO₂ nanocrystals with exposed {001} facets on graphene sheets via molecular grafting for enhanced photocatalytic activity, *Nanoscale* 4 (2012) 613–620.
- [14] Y.J. Lee, L.K. Putri, B.-J. Ng, L.-L. Tan, T.Y. Wu, S.-P. Chai, Blue TiO₂ with tunable oxygen-vacancy defects for enhanced photocatalytic diesel oil degradation, *Appl. Surf. Sci.* 611 (2023), 155716.
- [15] H. Sudrajat, A. Susanti, S. Hartuti, Reduced TiO₂ with prolonged electron lifetime for improving photocatalytic water reduction activity, *J. Phys. Condens* 35 (2023), 134001.
- [16] L. Pan, S. Sun, Y. Chen, P. Wang, J. Wang, X. Zhang, J.-J. Zou, Z.L. Wang, Advances in piezo-phototronic effect enhanced photocatalysis and photoelectrocatalysis, *Adv. Energy Mater.* 10 (2020) 2000214.
- [17] T. Zheng, J. Wu, D. Xiao, J. Zhu, X. Wang, X. Lou, Potassium–sodium niobate lead-free ceramics: modified strain as well as piezoelectricity, *J. Mater. Chem.* 3 (2015) 1868–1874.
- [18] Y. Gao, J. Zhang, Y. Qing, Y. Tan, Z. Zhang, X. Hao, Remarkably strong piezoelectricity of lead-free (K_{0.45}Na_{0.55})_{0.98}Li_{0.02}(Nb_{0.77}Ta_{0.18}Sb_{0.05})O₃ ceramic, *J. Am. Ceram. Soc.* 94 (2011) 2968–2973.
- [19] W. Tong, Y. Zhang, H. Huang, K. Xiao, S. Yu, Y. Zhou, L. Liu, H. Li, L. Liu, T. Huang, M. Li, Q. Zhang, R. Du, Q. An, A highly sensitive hybridized soft piezophotocatalyst driven by gentle mechanical disturbances in water, *Nano Energy* 53 (2018) 513–523.
- [20] S.R. Massel, Spectral and statistical properties of ocean waves, in: S.R. Massel (Ed.), *Ocean Waves Breaking and Marine Aerosol Fluxes*, Springer, New York, New York, NY, 2007, pp. 31–73.
- [21] J. Xing, H. Chen, L. Jiang, C. Zhao, Z. Tan, Y. Huang, B. Wu, Q. Chen, D. Xiao, J. Zhu, High performance BiFe_{0.9}Co_{0.1}O₃ doped KNN-based lead-free ceramics for acoustic energy harvesting, *Nano Energy* 84 (2021), 105900.
- [22] E.-P. Bao, S. Long, S. Zhang, H. Li, W. Zhang, J. Zou, Q. Xu, A. Ternary, Photocatalyst with double heterojunctions for efficient diesel oil degradation, *ChemistrySelect* 6 (2021) 3117–3125.
- [23] B.-J. Ng, L.K. Putri, X.Y. Kong, P. Pasbakhsh, S.-P. Chai, Overall pure water splitting using one-dimensional P-doped twinned Zn_{0.5}Cd_{0.5}S_{1-x} nanorods via synergetic combination of long-range ordered homojunctions and interstitial S vacancies with prolonged carrier lifetime, *Appl. Catal. B* 262 (2020), 118309.